

Defect-pinned nucleation, growth, and dynamic coalescence of Ag islands on MgO(001): An *in situ* grazing-incidence small-angle x-ray scattering study

C. Revenant,¹ G. Renaud,¹ R. Lazzari,² and J. Jupille²¹CEA, INAC, SP2M, NRS, F-38054 Grenoble, France²Institut des NanoSciences de Paris, Université Pierre et Marie Curie (Paris 6), CNRS UMR 7588, Campus Boucicaut, 140 rue de Lourmel, 75015 Paris, France

(Received 8 January 2009; revised manuscript received 20 April 2009; published 19 June 2009)

The growth of Ag/MgO(001) was investigated at three temperatures, 300, 540, and 640 K, *in situ*, in ultrahigh vacuum, by grazing incidence small angle x-ray scattering (GISAXS). The samples prepared at 300 and 540 K were also examined *ex situ* by transmission electron microscopy (TEM). Nucleation, growth, and coalescence are studied via the evolution of the average particle diameter, height, interparticle distance, and size distributions. Power laws are given. Size-spacing correlations are evidenced by TEM and GISAXS. A heterogeneous nucleation of silver on the defects [$(7.5 \pm 1.5) \times 10^{12}$ defects cm^{-2}] of the MgO surface is evidenced. Above a silver coverage of approximately 2 nm, a dynamic coalescence regime takes place involving diffusion of the islands. A value of 0.76 ± 0.1 J m^{-2} for the Ag/MgO(001) adhesion energy is derived by using a Wulff-Kaishew construction from the particle shape obtained by GISAXS. The diffusion energy of Ag on MgO(001) is estimated to be 0.05 ± 0.02 eV/atom via kinetic Monte Carlo simulations of the growth stage.

DOI: 10.1103/PhysRevB.79.235424

PACS number(s): 68.55.-a, 61.05.cf

I. INTRODUCTION

The growth of metallic nanoislands on oxide substrates relies on numerous atomistic mechanisms, including adsorption, re-evaporation, surface diffusion, and various kinds of interaction (metal-metal, metal-oxide, and metal defects). Its modeling requires to know whether nucleation occurs on defects and would ultimately allow to determine the characteristic energy of each phenomenon through a careful comparison with experiments.¹⁻⁴ On an experimental point of view, many different related questions have to be addressed to characterize the growth, among which are the type of nucleation, homogeneous or heterogeneous, the type of coalescence, static or dynamic, the atomic structure and epitaxial relationships of the supported metal clusters, the metal-substrate adhesion energy, the diffusion energy of the metal, and the relationship between the capture area and the island size.

The Ag/MgO(001) system is a model system because of the nonreacting character of both components and the cube/cube epitaxy which is due to a small (3%) lattice parameter mismatch. It is well established that Ag grows in a three-dimensional (3D) Volmer-Weber growth mode for all thicknesses. On-top adsorption on the oxide anion is found to be energetically preferred.⁵⁻⁷ The Ag islands are coherent, i.e., without interfacial dislocations up to an average thickness of ~ 0.8 nm.^{5,6} Theoretical studies were carried out to determine whether the nucleation of Ag on MgO is homogeneous,^{8,9} i.e., on regular sites, or heterogeneous, i.e., on defect sites. Ferrari and Pacchioni⁸ examined the interaction of Ag adatoms with surface vacancies of MgO. The surface point defects are mainly magnesium and oxygen vacancies, which lead to F_s and V_s centers, respectively.⁸ The Ag-surface bond, very weak on the regular sites, strongly depends on the formal charge of the vacancy. Zhukovskii *et al.*^{10,11} pointed out that Ag islands nucleate and grow mainly at defect sites. The strength of the adsorption of Ag adatoms

ranges from 9.6 eV/atom on V_s centers, to 2.1 eV/atom on F_s centers, and to 0.4 eV/atom on regular O^{2-} sites.¹² The diffusion energy of a silver atom on the MgO surface is evaluated theoretically to be 0.05 eV/atom,^{13,14} which is to be compared with the estimate of 0.01 eV/atom for the diffusion energy of Ag on Ag(111).¹⁵

The objectives of the present work are (i) to study the different stages of the growth, including nucleation, growth, and coalescence and (ii) to link these to the physical properties of the silver adlayer, namely, surface diffusion and adhesion energy. A special attention is paid to coalescence to determine whether it is static or dynamic.^{2,3,16-18} Addressing these issues requires the determination of the island morphology at all stages of the growth.

In the present work, analyses are performed by grazing incidence small angle x-ray scattering (GISAXS). The use of photons allows this technique to be run *in situ* and during the growth at a chosen substrate temperature, in an ultrahigh vacuum (UHV) environment and in the case of insulating substrates, without charging effects.¹⁹⁻²⁴ GISAXS performs a macroscopic sampling of the surface over the beam footprint, which amounts to several tens of microns times the sample size. It thus defines an average cluster, which corresponds to a statistical averaging over up to 10^{10} particles²⁵⁻³⁰ and a very high sensitivity.^{31,32} The growth of Ag/MgO(100) is studied from the very beginning (less than 0.1 nm) up to the later stages (several nanometers). After a presentation of the experimental details (see Sec. II), the diameter, height, interparticle distance, and size distributions are determined by a quantitative GISAXS analysis (see Sec. III). *Ex situ* transmission electron microscopy (TEM) is used to derive the interference function, which is needed to analyze GISAXS data. The nucleation, growth, and coalescence mechanisms are next discussed (see Sec. IV) on the basis of the evolution of the average morphological parameters of the film during the growth. Finally, the equilibrium shape and adhesion energy are determined as well as, with the help of a kinetic

Monte Carlo simulation (KMCS), the diffusion energy of Ag on MgO(001).

II. EXPERIMENTS

The measurements were performed at the European Synchrotron Radiation Facility (ESRF) on the ID32 undulator beamline,³³ on which a dedicated experimental setup was developed to perform GISAXS in UHV, *in situ*, during the growth of islands on a surface.³² The growth of Ag/MgO(001) was studied during two series of experiments. During the first series, silver was deposited at 540 K on a high quality MgO(001).³⁴ The $15 \times 15 \times 0.5$ mm³ MgO(001) substrate supplied by Earth Chemical Co., Ltd. (Tokyo, Japan) was first annealed at 1800 K in air for 24 h to improve its crystalline quality. Then, it was ion bombarded in a separated UHV chamber at the same temperature for 1 h to remove contaminants while keeping a flat and crystalline surface. The sample was next cooled down to room temperature under a partial oxygen pressure of 10^{-4} Torr and protected by a 100-nm-thick Ag buffer layer deposited by molecular beam epitaxy. The sample was finally glued onto the molybdenum holders with indium, transferred into the x-ray UHV chamber, and heated during typically 3 h around 900 K to desorb the Ag film, thus leaving a clean stoichiometric MgO(001) surface. Silver was deposited using a Knudsen cell operating at 1120 K under a pressure of 4×10^{-10} mbar on the MgO sample. The flux, $\sim 8 \times 10^{-3}$ ML/s, was calibrated *in situ* using a quartz microbalance. The monolayer (ML) corresponds to a Ag(100) atomic layer, i.e., 1.2×10^{15} Ag atoms cm⁻². The sample temperature was measured by using a pyrometer which emissivity was calibrated to the Mo surface of the sample holder since MgO is transparent to the collected wavelength. During the second series, the silver film was deposited at 300 and 640 K on MgO(001) in the same conditions except that the MgO(001) surface was prepared without annealing in air at 1800 K. As a consequence, the surface quality is not as good as the previous one and the surface may have more steps, nucleation centers, and roughness. The GISAXS measurements were performed at wavelengths of $\lambda=0.1210$ nm (300 and 640 K) and $\lambda=0.1127$ nm (540 K). In both cases, the angles of incidence were taken to be equal to the critical angles for total external reflection (0.20° and 0.22° , respectively). The scattering geometry and the definition of the wave-vector transfer were detailed elsewhere.^{35,36} The growth was analyzed simultaneously by surface differential reflectivity spectroscopy (SDRS) in the UV-visible range.³² The method is based on the excitation by the incident light of the plasmon resonances within the nanoparticle.³⁷ The quantitative SDRS analysis was previously compared to the GISAXS data.³⁸ Some of the samples were observed *ex situ* by TEM plane views with the carbon replica method. The samples were first encapsulated by an amorphous carbon layer. The MgO substrate was next dissolved by a selective chemical attack in diluted HCl (15%). The carbon film containing the particles was then mounted on microscope grids. The grids were observed at CRMCN (Marseille, France) in a Jeol 2000 FX electron microscope operating at 200 kV in transmission and diffraction modes.

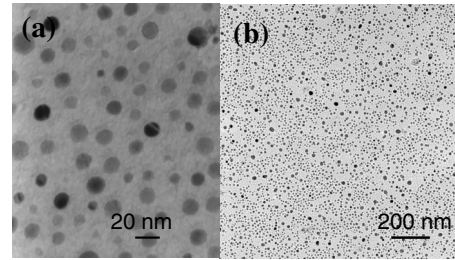


FIG. 1. TEM plane views after carbon replica of Ag/MgO(001) films deposited at (a) 300 K (10 nm Ag) and (b) 540 K (2 nm Ag).

III. RESULTS

A. Transmission electron microscopy results

Two GISAXS samples (10 and 2 nm deposited at 300 and 540 K, respectively) were later analyzed *ex situ* by TEM (Fig. 1). In the two cases, most clusters are seen by TEM diffraction to adopt the cube/cube [Ag(001)||MgO(001)] epitaxial relationship with a very good azimuthal orientation.⁶ Only a very small fraction of particles show the [Ag(111)||MgO(001)] epitaxy with azimuthal disorientations. At 300 K, the cluster density of the 10-nm-thick film is estimated to be $(1.3 \pm 0.2) \times 10^{11}$ cm⁻², which corresponds to an average interparticle distance L of 27.7 ± 2.2 nm. The particle shape is close to spherical with (111) side and (001) top facets. The average diameter D and aspect ratio H/D amount to 15 ± 1 nm and 0.9, respectively. In the case of the 2-nm-thick Ag film deposited at 540 K, a large-scale TEM picture was treated to extract the central in-plane size and its distribution. The cluster density is estimated to be $(4.4 \pm 0.3) \times 10^{11}$ cm⁻² which corresponds to an average interparticle distance L of 15.1 ± 0.5 nm. The lowest size of the clusters detected by TEM is approximately 2 nm. The lateral size histogram is shown in Fig. 2. It is fitted with a log-normal distribution defined by

$$p_{LN}(D) = \frac{1}{D\sqrt{2\pi\ln(\sigma/D_0)}} \exp\left\{-\frac{1}{2}\left[\frac{\ln(D/D_0)}{\ln(\sigma/D_0)}\right]^2\right\}, \quad (1)$$

where D is the lateral size and D_0 is the central value. The parameter σ is linked to the full width at half maximum of the distribution. The distribution has a central in-plane size

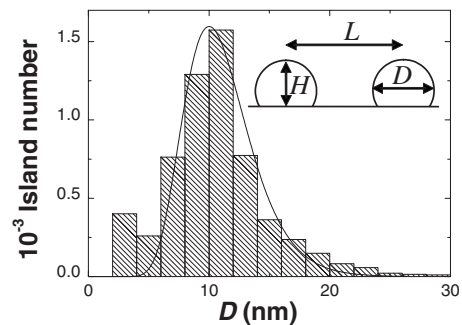


FIG. 2. Lateral size histogram of the 2-nm-thick Ag film deposited at 540 K, deduced from the TEM plane view displayed in Fig. 1(b). Inset: particles on a substrate with an interparticle distance L , a diameter D , and a height H .

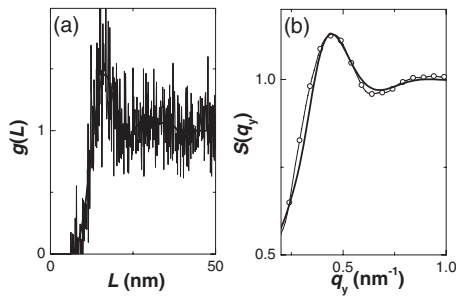


FIG. 3. (a) Pair correlation function $g(L)$. Thin line: experimental $g(L)$ deduced from the TEM image recorded at 540 K. Bold line: up to approximately 40 nm, smoothed experimental $g(L)$ with a low pass filter of 0.1 nm^{-1} ; above 40 nm, $g(L)$ was fixed at 1. The maximum of $g(L)$ is at $L=15.7 \text{ nm}$. (b) Open circles: interference function $S(q_y)$ obtained by Fourier transform of the experimental $g(L)$. Bold line: fitted $S(q_y)$ with an analytical function with two parameters L and ω (here, $L=15.7 \text{ nm}$, $\omega=7.5 \text{ nm}$) (Ref. 36). The maximum is at $q_y=0.45 \text{ nm}^{-1}$.

$D_0=10.5 \pm 0.5 \text{ nm}$ and a relative standard deviation $\sigma/D_0=1.3$. The size distribution is correctly accounted for by a log-normal function except for very small particles ($D \sim 2\text{--}5 \text{ nm}$), sketching a bimodal distribution. This point is discussed in Sec. IV D.

1. Interference function

The GISAXS data were first fitted by using the different model interference functions that were implemented in the ISGISAXS software used for the quantitative analysis.³⁵ However, none of them could account for (i) the shape of the first maximum of the GISAXS data parallel to the surface and (ii) the intensity evolution close to the origin of reciprocal space. We thus resorted to digitalized TEM plane views to define an *ad hoc* interference function. This method was previously found appropriate for the Pd/MgO system, for which it was described in detail.³⁶ The analysis was performed on large-scale pictures with a few thousands of clusters as in Fig. 1(b). The island-island pair correlation function $g(L)$ was derived, as well as its Fourier transform, the so-called interference function $S(q_y)$, where q_y is the wave-vector transfer component parallel to the surface (Fig. 3). $S(q_y)$ was fitted with the two-parameter (L as the interparticle distance and ω as a disorder parameter) function used for the Pd/MgO system.³⁶ This analytical function well fitted the experimental TEM-deduced interference function for Ag/MgO and Pd/MgO systems and was also satisfactorily tested for other systems with short-range order. These results were thus used to build a well-adapted interference function, mandatory for GISAXS data analysis.

2. Island correlation

A visual inspection of the TEM data displayed in Fig. 1 does not reveal any correlation between the sizes of neighboring islands. However, the nearest neighbors (NNs) of large islands look much farther away from this central island than those of small islands. These qualitative conclusions are confirmed by a detailed analysis of the TEM plane views,

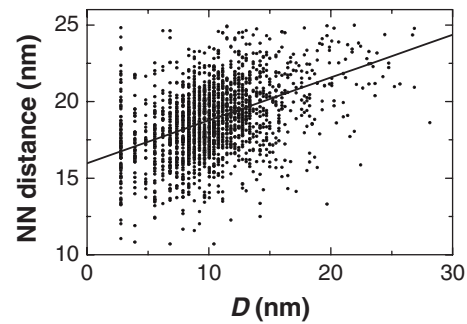


FIG. 4. Analysis of TEM image of the 2-nm-thick film Ag/MgO(001) grown at 540 K. The average distance between a central island and its nearest neighbors is reported as a function of the central-island diameter together with a least-squares fit to a straight line. Note that the limit for the NN distance is set to 25 nm because of the poor statistical relevance for higher values due to the finite size of the image.

which allows calculating the average diameter of NN islands as well as their separation from the central island as a function of the central island diameter. If no correlation between the sizes of NN islands is found, a clear correlation between the sizes of islands and the interisland distances is seen in Fig. 4, which is derived from the 2-nm-thick film deposited at 540 K. The linear regressions have positive slopes of 0.146 and 0.280 at 300 and 540 K, respectively, meaning that the larger the central island, the larger the distance from its NNs. This can be linked to the depletion zone which surrounds the islands, as directly observed on the TEM image in Fig. 1(b). Indeed, the islands grow via the diffusion of atoms from the depletion zone, leading to a scaling of the area of its Voronoi cell on its perimeter.³⁹ Then, in the coalescence regime, these Voronoi cells merge.

B. GISAXS results

Whatever the growth temperature, the two-dimensional (2D) GISAXS patterns look qualitatively similar. The series of patterns shown in Fig. 5 was recorded during the growth of the Ag/MgO(001) film at 540 K, with the incident x-ray beam oriented in the $[010]$ and $[1\bar{1}0]$ directions of the MgO(001) substrate, i.e., with q_y along the $[100]$ and $[110]$ directions [Figs. 5(a)–5(d) and Figs. 5(e)–5(h)], respectively. GISAXS provides an image in the reciprocal space of the geometry and spatial distribution of the supported particles.³⁶ The particle diameter D , height H , and interparticle distance L are derived from the width, height, and relative position in the parallel direction of the lobes seen on each side of the specular ($q_{\parallel}=0$) rod. Upon increasing coverage, the progressive shrinkage of the scattered pattern toward the origin of the reciprocal space reflects an increase in D , H , and L , which is characteristic of the growth and coalescence of the Ag islands.

When the incident x-ray beam is in the $[1\bar{1}0]$ direction as illustrated in Figs. 5(e)–5(h), whatever the deposition temperature, an additional scattering rod is observed at 54.7° relative to the surface normal, which is characteristic of the presence of (111) facets on the Ag islands. Already visible

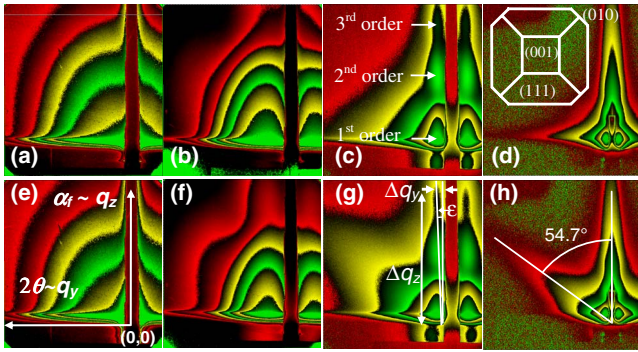


FIG. 5. (Color online) GISAXS patterns recorded *in situ* during the growth of Ag/MgO(001) at 540 K with the incident beam in the [(a)–(d)] [010] and [(e)–(h)] $\bar{1}\bar{1}0$ directions and for various coverages: [(a) and (e)] 0.1 nm, [(b) and (f)] 0.3 nm, [(c) and (g)] 2 nm, and [(d) and (h)] 7 nm. The intensity is represented on a logarithmic scale. Each black contour between two colors corresponds to 1 order of magnitude change in intensity. The q_y (q_z) axis ranges from 0 to 2.7 nm^{-1} (3 nm^{-1}). Inset in (d): top view of the truncated cubo-octahedron particle shape with (001), (111), and (010) facets.

for a coverage of 0.3 nm, it becomes more intense as the thickness increases. Moreover, a second- and even a third-order maxima appear in the q_z direction as indicated in Fig. 5(c). They correspond to clusters with (i) top (001) facets and (ii) a narrow distribution of heights. At higher coverage, these maxima disappear under the specular rod. The GISAXS pattern then looks like an apex, meaning that the islands become even flatter and evolve toward large and flat clusters, which expose a top {001} surface and side {111} facets.⁴⁰ An additional feature is deduced from Fig. 5 by comparing Figs. 5(c) and 5(d) to Figs. 5(g) and 5(h). The intensity in the q_y direction at the Yoneda peak position is clearly larger (weaker) when the beam is in the [010] [$\bar{1}\bar{1}0$] direction. This indicates an additional scattering rod in the [010] direction, characteristic of {100} facets. These {100} facets appear for a Ag coverage as small as 2 nm and grow as the Ag coverage increases from 2 to 7 nm. All these features are consistent with a truncated cubo-octahedron shape with {111} and {100} facets represented in the inset of Fig. 5(d).

1. GISAXS data analysis

Extracting precise morphological parameters from GISAXS data needs the use of an appropriate model, which should account for the shape of the clusters, the distributions of sizes, and the island-island pair correlation function, as well as the refraction effects when the incident or exit angles are close to the critical angle for total external reflection.^{41–43} However, this is at the cost of the computational burden. To ease the analysis, the GISAXS data were all analyzed by means of a simplified method called rapid data analysis.^{38,44,45} By means of the ISGISAXS software, it allows a quantitative GISAXS analysis of a large variety of systems,³⁵ such as metallic islands,^{36,46} gradient nanoparticle-polymer multilayer,^{47,48} Ge nanoparticles,^{49,50} self-organized nanodot pattern,⁵¹ or faceted surface.⁵² For the sake of comparison as well as for an accurate determination

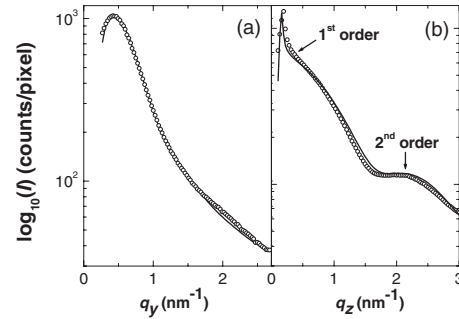


FIG. 6. GISAXS cut (a) parallel to the surface at the position of maximum intensity, i.e., $q_z=0.16 \text{ nm}^{-1}$, and (b) perpendicular to the surface at the position of maximum intensity, i.e., $q_y=0.46 \text{ nm}^{-1}$, for the 1-nm-thick deposit of Ag/MgO(001) at 540 K. Open circles: cut of the experimental GISAXS pattern; line: best fit of the experimental cut with the extensive data analysis. The intensity is represented on a logarithmic scale.

of the cluster morphology, the complete quantitative analysis was performed in a few cases in the present study. The clusters were modeled by truncated octahedra, as suggested by the examination of the GISAXS patterns (Fig. 5), with lateral and vertical size distributions described by log-normal probabilities. Calculations were done in the framework of the distorted wave Born approximation and of the local monodisperse approximation. Figure 6 gives an example of a simultaneous fit to two intensity cuts of the GISAXS data. One cut is parallel to the surface at the q_z position of maximum intensity and the other is perpendicular to it at the q_y position of the interference maximum. The model nicely accounts for all experimental features, in particular, the interference function deduced from TEM fits very well with the GISAXS maximum in the parallel cut.

The average values of L , D , and H are plotted in Fig. 7 for films grown at 300, 540, and 640 K. This D (H) value is the average of D (H) over the lateral (vertical) size distribution. For the rapid data analysis, the error bars are $\Delta L/L=15\%$, $\Delta D/D=30\%$, and $\Delta H/H=20\%$. For the extensive data analysis, the error bars are $\Delta L/L=10\%$, $\Delta D/D=20\%$, and

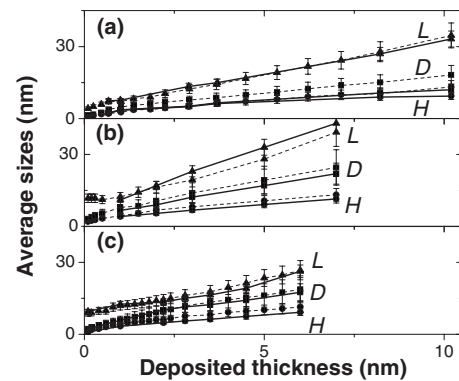


FIG. 7. Evolution of average sizes obtained from the GISAXS measurements for Ag on MgO(001). Up triangles: interparticle distance L ; filled squares: island diameter D ; and filled circles: island height H . Dash: rapid data analysis; thick line: extensive data analysis. (a) 300 K; (b) 540 K; and (c) 640 K.

$\Delta H/H=15\%$. The relative standard deviation of the log-normal size distribution of the Ag islands was deduced from the extensive GISAXS data analysis as a function of the film thickness for the three substrate temperatures. The σ_D/D and σ_H/H parameters of the log-normal diameter and height distributions range between 1.1 and 1.4 and between 1.1 and 1.2, respectively. The average distance and diameter determined by TEM for the 10-nm-thick Ag film at 300 K ($L=27.7$ nm and $D=15$ nm) and for the 2-nm-thick Ag film at 540 K ($L=15.1$ nm and $D=10.5$ nm) (see Sec. III A) are in good agreement with the results obtained from the extensive data analysis in the same conditions ($L=33$ nm and $D=12$ nm for a 10-nm-thick film at 300 K; $L=16$ nm and $D=10$ nm for 2 nm at 540 K). The rapid analysis mostly overestimates the length values with respect to the full quantitative analysis. If interparticle distances only differ by 15%, the relative difference between H (D) is much larger and can reach 30% (35%). This discrepancy likely comes from the models. In the rapid data analysis, the average island is modeled by an arbitrary shape without any size distribution while the extensive data analysis involves a realistic shape with a size distribution. Unless mentioned, the results that are displayed hereafter are obtained with the rapid data analysis.

2. Size-position correlation deduced from GISAXS

A close examination of the GISAXS data displayed in Figs. 5(c) and 5(g) reveals that the second- and third-order maxima often show a faint positive tilt with respect to the q_z axis. Indeed, the slope of the third-order peak is characterized by an angle ε with respect to the q_z axis, with

$$\tan(\varepsilon) = \frac{\Delta q_y}{\Delta q_z}. \quad (2)$$

The parameters Δq_y , Δq_z , and ε are shown in Fig. 5(g). To a first approximation, $L \sim 2\pi/q_{y \max}$, where $q_{y \max}$ is the q_y coordinate of maximum intensity. By derivation, it comes

$$\frac{\Delta q_y}{q_{y \max}} = \frac{\Delta L}{L}. \quad (3)$$

If the cluster is modeled by a simple shape such as a cylinder, the form factor is equal to

$$F_{cy} = (q, R, H) = 2\pi R^2 H \frac{J_1(q_{\parallel} R)}{q_{\parallel} R} \text{sinc}(q_z H/2) \exp(-i q_z H/2),$$

$$q_{\parallel} = (q_x^2 + q_y^2)^{1/2}.$$

If the refraction effects are neglected, the intensity along q_z is proportional to the square of $\text{sinc}(q_z H/2)$. Hence, one obtains $H \sim (5/2) \times \pi/q_{z \max}$, where $q_{z \max}$ is the q_z position of the third-order maximum. Thus,

$$\frac{\Delta q_z}{q_{z \max}} = \frac{\Delta H}{H}. \quad (4)$$

For the growth at 540 K, the aspect ratio H/D is approximately 0.6 [Fig. 7(b)], whatever the deposited thickness. Hence,

$$\frac{\Delta H}{H} = \frac{\Delta D}{D}. \quad (5)$$

Combining the different equations finally yields

$$\frac{\Delta L}{\Delta D} = \frac{5}{4} \tan(\varepsilon) \frac{L^2}{DH}. \quad (6)$$

In the case of the 2-nm-thick Ag/MgO film at 540 K [Figs. 5(c) and 5(g)], $\tan(\varepsilon)=0.04 \pm 0.01$ and hence with $L=17$ nm, $D=9$ nm, and $H=5.5$ nm [Fig. 7(b)], $\Delta L/\Delta D=0.29 \pm 0.05$

Therefore, the tilt of the GISAXS maxima with respect to the q_z direction arises from a correlation between the particle size and the interparticle spacing. In addition, it provides an estimate of the correlation parameter ($\Delta L/\Delta D$) between the size and the separation of islands. In the present case, the excellent agreement between TEM (0.28) and GISAXS (0.29 ± 0.05) leads to a very reliable value of that parameter for the Ag/MgO(001) films.

IV. DISCUSSION

The evolution of the average morphological parameters allows a description of the nucleation, growth, and coalescence of the silver growth on MgO(001). Then, an estimate of the diffusion energy is derived from a kinetic Monte Carlo modeling and the equilibrium shape of the silver clusters is determined by means of the GISAXS data.

A. Quantitative character of the GISAXS measurement

Because it is based on the diffraction laws, GISAXS is a reliable method. Nevertheless, the comparison, which was previously made between GISAXS and SDRS analyses, leads to a better knowledge of the strengths and limits of both methods.³⁸ For different reasons, these have difficulties to detect very small clusters. While the aperture of the GISAXS detector is limited to particles typically larger than 1 nm, the blueshift of the SDRS response of small silver particles is not easy to model.⁵³ To first approximation, beyond that lower limit, the SDRS signal depends linearly on the film thickness⁵⁴ and the SDRS thickness well agrees with the quartz-balance measurement.³⁸ Instead, the thickness derived from the GISAXS analysis levels off above approximately 4 nm. Hence, the limit of the calculated thickness obtained from the GISAXS data has its origin in the GISAXS technique itself. Due to the way the average thickness is calculated from GISAXS data ($\sim HD^2L^{-2}$), small shifts in D and L values strongly affect the thickness estimate. Moreover, the scattered x-ray beam is collected outside the beam stop and within the detector aperture, imposing not only a lower value (≈ 1 nm) but also an upper value of the particle size. For example, in the geometry used at 300 K, GISAXS probes particles only up to 18 nm. Then, larger clusters escape the GISAXS detection, explaining the behavior of the GISAXS signal above an average thickness of 4 nm.

On the positive side of the parallel study of GISAXS and SDRS, an extremely important conclusion was that both

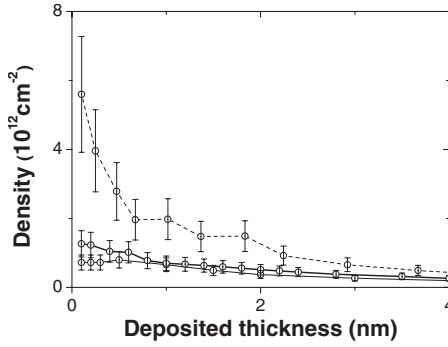


FIG. 8. Island density obtained from GISAXS versus a function of the silver thickness. Dash: $T=300$ K; thin line: $T=540$ K; and thick line: $T=640$ K.

methods almost perfectly agree on the values of aspect ratios H/D at all temperatures and coverages.³⁸ Indeed, because of the physics behind SDRS and GISAXS, the parameter H/D is directly determined in both SDRS (Ref. 55) and GISAXS (straightforward from the principle of the method). Then, provided the thickness of the Ag(100)/MgO(100) film is lower than 4 nm, the GISAXS analysis yields reliable information on the morphology of the silver particles.

B. Heterogeneous nucleation on defects

The interparticle distance yields an estimate of the particle density calculated by $1/L^2$ and displayed in Fig. 8. At the very beginning of growth (Ag-deposited thickness of approximately 0.1 nm), the particle densities are approximately $6 \times 10^{12} \text{ cm}^{-2}$ at 300 K and $1.3 \times 10^{12} \text{ cm}^{-2}$ at 640 K (Fig. 8). The corresponding SDRS values ($8.6 \times 10^{12} \text{ cm}^{-2}$ at 300 K and $4.9 \times 10^{12} \text{ cm}^{-2}$ at 640 K) are slightly higher than the GISAXS ones.³⁸ The smaller GISAXS values at low coverage are assigned to the existence of clusters too small (typically < 1 nm) to be detected by GISAXS.³⁸ Such densities are characteristic of a heterogeneous nucleation on defects, with a defect concentration given by the low-temperature value of $\sim (7.5 \pm 1.5) \times 10^{12} \text{ defects/cm}^2$ (average from SDRS and GISAXS). Haas *et al.*⁵⁶ came to a similar estimate for Pd/MgO(001). They found a constant island density ($\sim 3 \times 10^{12} \text{ cm}^{-2}$) by atomic force microscopy which was assigned to nucleation kinetics governed by point defects with a high trapping energy. A similar idea was also used to explain the maximum cluster density of Co on Au(788) over a large range of temperature.⁵⁷

C. Power laws for growth and dynamic coalescence of silver clusters

Insight in the Ag growth and coalescence modes is gained by studying the evolution of the interparticle distance L , the diameter D , and the height H versus the coverage, which is the fraction of the substrate covered by clusters, in a \log_{10} - \log_{10} plot shown in Fig. 9. The coverage is represented by the time of exposure at constant flux since, on the basis of SDRS measurements, the sticking probability of Ag on the MgO(001) surface is assumed to be constant and equal to

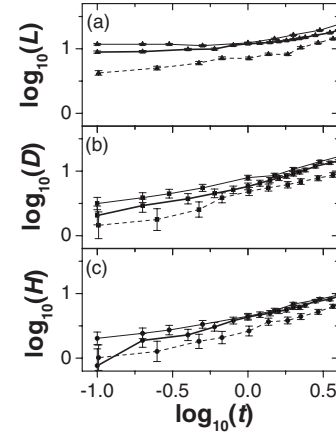


FIG. 9. \log_{10} - \log_{10} plot of (a) L , (b) D , and (c) H obtained by GISAXS as a function of time for different deposition temperatures. The parameter t is the Ag-deposited thickness. Dash: $T=300$ K; thin line: $T=540$ K; and thick line: $T=640$ K.

unity.³⁸ Explicitly, the Ag thickness in ML is the flux in ML/s multiplied by the time of exposure in s.

In Fig. 9, a break in slope of the interparticle distance L occurs for a thickness of approximately 2 nm. It suggests the existence of two different regimes. Below and above this value, the parameters L and D can be modeled by a power law of t . Below 2 nm, the interparticle distance L increases according to a power law $\sim t^n$ with $n \sim 0.1-0.2$ (Table I). Meanwhile, the particle diameter D increases according to a power law $\sim t^m$ with $m \sim 0.3-0.4$. The m exponent is less accurate than n due to the larger error bars of D compared to those of L at small t . This m value indicates that particles grow by capture of diffusing species in their surface of influence with a negligible direct impingement.^{58,59} Between density saturation and coalescence, the $m \sim 1/3$ exponent is characteristic of a surface with a high defect concentration.⁶⁰ This is consistent with the findings of Sec. IV B.

In a nonconserved mass system, two main coalescence mechanisms are often invoked to describe the arrival of new material on the surface, either static or dynamic.^{2,3} In static coalescence, neighboring growing islands merge when they touch, leading to a new island occupying the center of mass of the two primary islands. In all theoretical studies, the coalescence time and the reshaping time are supposed to be very small compared to the arrival time of incoming atoms so that the islands are supposed to keep always the same shape. By contrast, dynamic coalescence involves the diffusion of islands (in the form of clusters of adatoms or small particles)

TABLE I. Exponent values of $L \sim t^n$ and $D \sim t^m$ in the growth and coalescence regimes at different temperatures.

T (K)	Coverage < 2 nm		Coverage > 2 nm	
	n	m	n	m
300	0.2 ± 0.03			
540	0.1 ± 0.02	0.33 ± 0.1	0.7 ± 0.1	0.6 ± 0.2
640	0.1 ± 0.02			

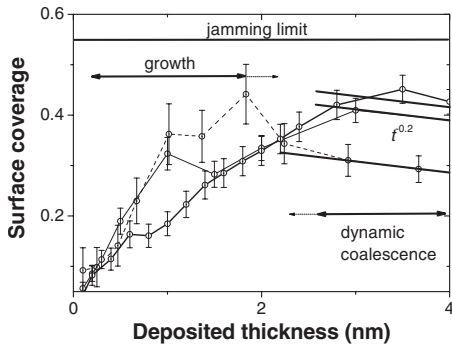


FIG. 10. Surface coverage derived from GISAXS data as a function of the film thickness t . Dash: $T=300$ K; thin line: $T=540$ K; and thick line: $T=640$ K. For films thicker than 2–3 nm, the surface coverage obeys a $t^{-0.2}$ behavior.

on the surface. Ag islands can be mobile on some substrates.^{16,17} Deltour *et al.*¹⁸ showed that nonepitaxial or noncoherent large islands can diffuse rapidly. At variance, the cost in energy for diffusion seems to lock coherent particles. For films thicker than 2 nm, $L \sim t^n$ with $n \sim 0.7$ and $D \sim t^m$ with $m \sim 0.6$ whatever the temperature range (Table I). This regime can be assigned to a dynamic coalescence process with a surface coverage, defined by the island density multiplied by the surface occupied by one island, i.e., $(\pi/4) \times D^2/L^2$, obeying a $t^{-0.2}$ behavior, whatever the temperature (cf. Fig. 10). This behavior is in agreement with a $t^{2(m-n)}$ behavior. The surface coverage is comprised between 25% and 45% (Fig. 10). It is well below the jamming limit of 55%.^{3,61} A static coalescence process would yield a $D \sim t^1$ power law. It can be ruled out.^{58,62,63} Several authors investigated the dynamic coalescence of 3D particles on a 2D substrate. Particularly interesting is the work of Meakin⁶³ who carried out simulations of Brownian diffusion limited coalescence of droplets in which the droplet diffusion coefficient scales with their volume as $D_F \sim (D/2)^{3\gamma}$. Although Meakin dealt with systems with fixed mass, his model shades light on the present case. He found a logarithmic correction for the power law of the droplet diameter $D \sim [t/\ln(t)]^{1/3(1-\gamma)}$ and for the interparticle distance $L \sim [t/\ln(t)]^{1/2(1-\gamma)}$. The Ag/MgO(001) data are satisfactorily fitted with these laws by using $\gamma \sim 0.8$. This positive value corresponds to an enhanced diffusion of the largest islands contrary to what is expected from standard models of epitaxially matched particles.⁶⁴ Notably, in this coverage range, the Ag clusters are no longer in coherent registry with MgO(001). They display interfacial dislocations,⁶ which may make the diffusion easier than in the case of coherent particles.¹⁸ A similar behavior was already described for Au/Al₂O₃ by combining TEM and simulation,^{65,66} Pd/MgO(001),⁶⁷ and Au/TiO₂(110).⁵⁹

In Fig. 9, the clusters grown at 540 K are bigger than those deposited at 640 K at the same coverage. This apparent unphysical behavior is attributed to the difference in surface preparation since experiments at 540 K were not performed on the same surface as experiments at 300 and 640 K (see Sec. II). Most importantly, that difference does not have any effect on the exponents of the power laws which account for growth and coalescence and which are the aim of the present study (Table I).

D. Estimate of the diffusion energy of Ag on MgO(001) by KMCS

In the growth regime, the incoming Ag atoms diffuse on the MgO(001) substrate until they hit an island. Hence, this regime is controlled by the diffusion of Ag on MgO(001). To determine the corresponding diffusion energy E_d , the growth is modeled by kinetic Monte Carlo simulation up to a coverage of 2 nm (see Sec. IV D).^{65,66} The assumptions, partly based on the above findings, are the following. (i) Ag atoms are deposited randomly on the MgO surface at a constant rate, 1.09×10^{-2} and 5.27×10^{-3} ML s⁻¹ at 300 and 640 K, respectively, where 1 ML corresponds to 1.2×10^{15} Ag atoms cm⁻². (ii) Ag atoms can diffuse on the MgO(001) surface following the Arrhenius law $\tau = v_0^{-1} \exp(E_d/kT)$, where τ is the mean time between two jumps, v_0 is the attempt frequency (fixed at 10^{12} s⁻¹), k is the Boltzmann constant, and T is the temperature in kelvin. (iii) The defects are distributed randomly on the MgO surface. They are assumed to trap the atoms perfectly since the adsorption energy of Ag atoms on defects is predicted to be very high, i.e., from 2 to 10 eV/Ag adatom according to the defect type.¹² The defect concentration is $n_t = 6.7 \times 10^{-3}$. (iv) The islands have a truncated spherical-like shape with the aspect ratio H/D found in GISAXS. (v) If two islands get in contact, they coalesce instantaneously. In this regime, below 2 nm, the coalescence is indeed assumed to be static in agreement with the formation of a coherent interface.^{5,6} The results of some KMCS simulations are shown in Fig. 11 for the cases of a 1-nm-thick Ag(100)/MgO(100) film at 300 and 640 K and of a 2-nm-thick film at 640 K.

The KMCS yields a bimodal size distribution. The KMCS medium-size distribution is in good agreement with the GISAXS results (Fig. 11). On the contrary, the distribution of small clusters that appears in KMCS is not detected by GISAXS. The average size of small clusters (<1.5 nm) is close to the limit of detection of GISAXS (see Sec. IV A). Indeed, the ratio between the medium and small lateral sizes is typically 5 (Table II). Hence, the small island distribution corresponds to a negligible proportion ($\sim 1\%$) of the total amount of silver. Therefore, the small size distribution, which cannot be detected by GISAXS, is quantitatively marginal. Nevertheless, the bimodal distribution predicted by KCMS has a physical significance and, from that point of view, it cannot be neglected. Then, it is nice to observe that the size distribution derived from TEM data shows some kind of bimodal shape, consistent with the KCMS prediction (see Sec. III A and Fig. 2).

The overall agreement between experiment and simulation on the size distribution (right panel of Fig. 11) raises the confidence about the above assumptions, in particular, the nucleation on defects. The best agreement between the KMCS and GISAXS medium-size distributions is obtained with a diffusion energy E_d of 0.05 ± 0.02 eV $\cong 0.09$ J/m², which corresponds to a very-high mobility. The diffusion energy of Ag atoms on MgO(001) surface is determined on the basis of experimental observations. This value is in perfect agreement with that obtained by Fuks *et al.* by an *ab initio* calculation at 1/4 coverage for a Ag jump between two neighboring silver atoms sitting on surface oxygen atom in a

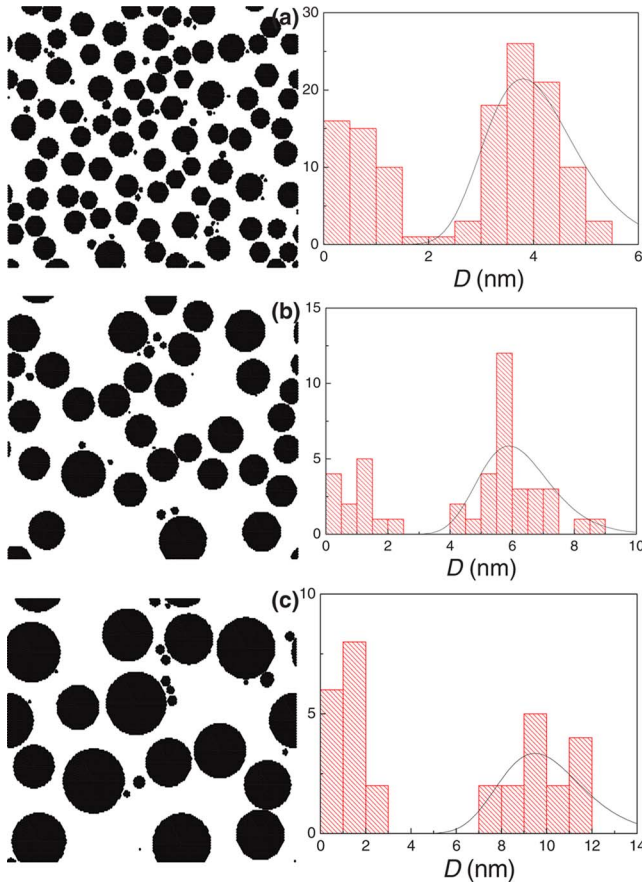


FIG. 11. (Color online) KMCS results displaying a top view of the Ag/MgO(001) films and the particle-size distribution at (a) 300 K, coverage of 1 nm, and (b) 640 K, coverages of 1 nm and (c) 2 nm. The size of the images is $64 \times 55.5 \text{ nm}^2$. The size histogram corresponds to the KMCS results and the line corresponds to the GISAXS results.

position of nearest neighbors on the MgO(100) surface (for alternative diffusion pathway between nearest O and Mg atoms, the diffusion barrier is almost three times larger).¹³

E. Equilibrium island shape and interfacial energy

GISAXS yields unique *in situ* and nondestructive information on the shape of the supported clusters. By means of

TABLE II. Estimates of the central values of the KMCS results obtained at different temperatures: diameter of the small islands (D_s) and diameter of the medium islands (D_m). Ratio of the diameters (D_m/D_s), estimate of the ratio of the medium island volume (V_m) and of the small island volume (V_s), and estimate of percentage of the total volume that corresponds to the small island volume.

T (K)	D_s (nm)	D_m (nm)	D_m/D_s	V_m/V_s	$V_s/(V_m+V_s)$ (%)
300	0.75	3.75	5	125	0.8
540	1.25	5.75	4.6	97	1
640	1.50	9.50	6.3	250	0.4

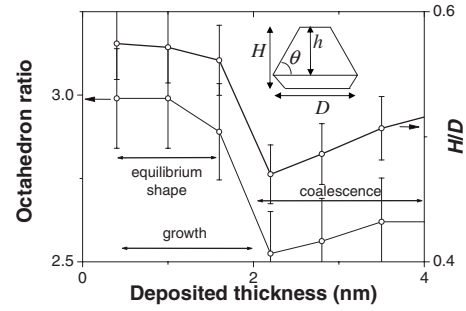


FIG. 12. Evolution of the island shape as a function of the deposited thickness at 640 K. Thin line: octahedron ratio, i.e., $h/(H-h)$ with Y axis on the left hand side; thick line: H/D with Y axis on the right-hand side. Inset: side view of a truncated octahedron.

the quantitative ISGISAXS software, the GISAXS analysis is performed with a silver cluster modeled by a truncated octahedral shape (see Sec. III B). The cluster is characterized by its aspect ratio H/D and by the ratio $r_H = h/(H-h)$ of the height h on the top of the octahedron over the height ($H-h$) on the bottom of the octahedron (see inset in Fig. 12). At 640 K, Fig. 12 shows that both the island aspect ratio H/D and the octahedron ratio r_H are constant in the 0.4–1.6 nm coverage range. This indicates that the islands have reached their equilibrium shape or are close to. The truncated octahedron used in the GISAXS simulation is a good approximation to the truncated cubo-octahedron described in the literature.¹ The adhesion energy β can then be determined by using the Wulff-Kaishew construction^{68,69} via the equation

$$\beta = 2\sigma_{(001)} \left[1 - \frac{H}{D} \times \frac{\sigma_{(111)}}{\sigma_{(001)}} \times \frac{1}{\sin(\theta)} \right], \quad (7)$$

in which $\sigma_{(001)} = 1.20 \text{ J m}^{-2}$ and $\sigma_{(111)} = 1.17 \text{ J m}^{-2}$ are the surface energies of the (001) and (111) facets and $\theta (54.7^\circ)$ is the angle between them.⁷⁰ Taking $H/D = 0.57$ yields $\beta = 0.76 \pm 0.1 \text{ J m}^{-2}$, which is in excellent agreement with the value of $0.75 \pm 0.1 \text{ J m}^{-2}$ deduced from the SDRS measurements.³⁸ Since the adhesion energy depends on the nature and concentration of surface defects,⁷¹ it is worth noticing the consistency of our results derived of *in situ* SDRS and GISAXS data collected simultaneously.

Indeed, other experimental values are 0.45 J m^{-2} (Ref. 40) and $0.3 \pm 0.3 \text{ J m}^{-2}$ (Ref. 72) which differ from the present value. However, they may derive from data recorded on substrates with different defect concentrations. Indeed, in the absence of a strict control of the surfaces, the meaning of the absolute values of the adhesion energy is questionable. Numerous theoretical values of the adhesion energies of Ag/MgO(001) were reported previously: 1.6 J m^{-2} on the basis of density-functional theory,⁷³ 0.64 J m^{-2} from electronic-structure total-energy investigations,⁷⁴ 0.95 J m^{-2} for impurity-free Ag/MgO(001) from fully self-consistent all-electron density-functional calculations,⁷⁵ and 0.45 J m^{-2} .⁷⁶ Purton *et al.*⁷⁷ reported 0.26 J m^{-2} for an ideal interface from atomistic simulations and they demonstrated that charged defects and impurities play an important role in

metal-ceramic adhesion. Zhukovskii^{10,11} found 0.83 J m^{-2} for three silver layers on MgO(001) using Hartree-Fock calculations. Those values are scattered over a too large range to be compared to the experiment.

In the 1.6–2.2 nm thickness range, the decrease in the aspect ratio H/D means that the islands become flatter. This is consistent with the growth by capture of the species diffusing in the surface of influence of the cluster with a negligible direct impingement (see Sec. IV C). Indeed, while the side $\{111\}$ facets grow from both vapor phase and atom diffusion, the top $\{001\}$ facet grows mostly from the vapor phase because of the high energy barrier that is encountered by atoms to jump from a $\{111\}$ to a $\{001\}$ facet.^{78,79} Then, above 2.2 nm, in the coalescence regime, the ratio H/D increases. The limiting step of the relaxation following the coalescence is the nucleation of a germ of the size of the smallest facet on a larger facet.^{80,81} In the cubo-octahedron, the larger facets are $\{001\}$ and $\{111\}$ facets. Due to experimental uncertainties, GISAXS does not allow distinguishing which facet among $\{001\}$ or $\{111\}$ is the largest. The increase in the H/D ratio would indicate that the island growth occurs preferentially on a $\{001\}$ facet, which would then be the largest facet of the cubo-octahedron.

V. CONCLUSION

The evolution of the Ag island morphology was investigated *in situ*, during the growth, by GISAXS and *ex situ* by TEM. The combination of both techniques allowed us to fully characterize the shape, size, size distribution, and average separation of the growing islands. A rapid GISAXS

analysis was found to provide a rough estimate of the average dimensional parameters, but a complete quantitative analysis is necessary if more precise values or the size distributions are needed. A clear correlation due to the diffusion processes was found between sizes and separation of neighboring islands. The larger the island is, the farther its nearest-neighbor islands.

The evolutions of the dimensional parameters with increasing thickness were analyzed in terms of nucleation density and power laws. A heterogeneous nucleation on defects [$(7.5 \pm 1.5) \times 10^{12} \text{ defects cm}^{-2}$] was evidenced. Following a detailed GISAXS analysis to derive the shape of the silver clusters, the adhesion energy ($0.76 \pm 0.1 \text{ J m}^{-2}$) was determined by means of the Wulff relation. KMCS of the growth regime (up to a thickness of typically 2 nm) allowed the determination of the diffusion energy of Ag adatoms on MgO(001), i.e., $E_d = 0.05 \text{ eV/atom}$. Above a silver thickness of approximately 2 nm, there is a regime of dynamic coalescence with enhanced diffusion of large islands on the MgO surface.

ACKNOWLEDGMENTS

We thank Claude R. Henry for providing the TEM plane views displayed in this study, J.-L. Maurice for allowing us to use the KMCS software, and Julian Carrey for helping us to cope with this software. We also thank all the staff of the ESRF ID32 beamline for their invaluable help during the GISAXS setup and measurements. We acknowledge support by the University Joseph Fourier, Grenoble, France to which the SP2M laboratory is associated.

¹C. R. Henry, Surf. Sci. Rep. **31**, 231 (1998).

²M. Zinke-Allmang, L. C. Feldman, and M. H. Grabow, Surf. Sci. Rep. **16**, 377 (1992).

³M. Zinke-Allmang, Thin Solid Films **346**, 1 (1999).

⁴J. Venables, *Introduction to Surface and Thin Film Processes* (Cambridge University Press, Cambridge, 2000).

⁵G. Renaud, Surf. Sci. Rep. **32**, 5 (1998), and references therein.

⁶O. Robach, G. Renaud, and A. Barbier, Phys. Rev. B **60**, 5858 (1999).

⁷A. M. Flank, R. Delaunay, P. Lagarde, M. Pompa, and J. Jupille, Phys. Rev. B **53**, R1737 (1996).

⁸A. M. Ferrari and G. Pacchioni, J. Phys. Chem. **100**, 9032 (1996).

⁹A. V. Matveev, K. M. Neyman, I. V. Yudanov, and N. Rösch, Surf. Sci. **426**, 123 (1999), and references herein.

¹⁰Y. F. Zhukovskii, M. Alfredsson, K. Hermansson, E. Heifets, and E. A. Kotomin, Nucl. Instrum. Methods Phys. Res. B **141**, 73 (1998).

¹¹Y. F. Zhukovskii, E. A. Kotomin, P. W. M. Jacobs, A. M. Stoneham, and J. H. Harding, J. Phys.: Condens. Matter **12**, 55 (2000).

¹²Y. F. Zhukovskii and E. A. Kotomin, Phys. Status Solidi C **2**, 347 (2005), and references herein.

¹³D. Fuks, S. Dorfman, E. A. Kotomin, Y. F. Zhukovskii, and A.

M. Stoneham, Phys. Rev. Lett. **85**, 4333 (2000).

¹⁴E. A. Kotomin, V. N. Kuzovkov, G. Zvejnieks, Y. Zhukovskii, D. Fuks, S. Dorfman, and A. M. Stoneham, Solid State Commun. **125**, 463 (2003).

¹⁵H. Brune, K. Bromann, H. Röder, K. Kern, J. Jacobsen, P. Stoltze, K. Jacobsen, and J. Nørskov, Phys. Rev. B **52**, R14380 (1995).

¹⁶J.-M. Wen, S.-L. Chang, J. W. Burnett, J. W. Evans, and P. A. Thiel, Phys. Rev. Lett. **73**, 2591 (1994).

¹⁷I. M. Goldby, L. Kuipers, B. von Issendorf, and R. E. Palmer, Appl. Phys. Lett. **69**, 2819 (1996).

¹⁸P. Deltour, J.-L. Barrat, and P. Jensen, Phys. Rev. Lett. **78**, 4597 (1997).

¹⁹B. M. Lairson, A. P. Payne, S. Brennan, N. M. Rensing, B. J. Daniels, and B. M. Clemens, J. Appl. Phys. **78**, 4449 (1995).

²⁰O. Malis, J. D. Brock, R. L. Headrick, M.-S. Yi, and J. M. Pomeroy, Phys. Rev. B **66**, 035408 (2002).

²¹A. Gibaud, S. Dourdain, O. Gang, and B. M. Ocko, Phys. Rev. B **70**, 161403(R) (2004).

²²R. E. Winans, S. Vajda, B. Lee, S. J. Riley, S. Seifert, G. Y. Tikhonov, and N. A. Tomczyk, J. Phys. Chem. B **108**, 18105 (2004).

²³S. V. Roth, T. Autenrieth, G. Grübel, C. Riekkel, M. Burghammer, R. Hengstler, L. Schulz, and P. Müller-Buschbaum, Appl. Phys.

- Lett. **91**, 091915 (2007).
- ²⁴T. Sun, H. Hu, Z. Pan, X. Li, J. Wang, and V. P. Dravid, *Phys. Rev. B* **77**, 205414 (2008).
- ²⁵J. R. Levine, J. B. Cohen, Y. W. Chung, and P. Georgopoulos, *J. Appl. Crystallogr.* **22**, 528 (1989).
- ²⁶J. R. Levine, J. B. Cohen, and Y. W. Chung, *Surf. Sci.* **248**, 215 (1991).
- ²⁷A. Naudon, T. Slimani, and P. Goudeau, *J. Appl. Crystallogr.* **24**, 501 (1991).
- ²⁸A. Naudon and D. Thiaudière, *J. Appl. Crystallogr.* **30**, 822 (1997).
- ²⁹D. Thiaudière, O. Proux, J.-S. Micha, C. Revenant, J.-R. Regnard, and S. Lequien, *Physica B* **283**, 114 (2000).
- ³⁰D. Babonneau, M.-F. Beaufort, A. Declémy, J.-F. Barbot, and J.-P. Simon, *J. Appl. Phys.* **99**, 113507 (2006).
- ³¹G. Renaud, R. Lazzari, C. Revenant, A. Barbier, M. Noblet, O. Ulrich, F. Leroy, J. Jupille, Y. Borensztein, C. R. Henry, J.-P. Deville, F. Scheurer, J. Mane-Mane, and O. Fruchart, *Science* **300**, 1416 (2003).
- ³²G. Renaud, M. Ducruet, O. Ulrich, and R. Lazzari, *Nucl. Instrum. Methods Phys. Res. B* **222**, 667 (2004).
- ³³<http://www.esrf.eu/UsersAndScience/Experiments/SurfaceScience/ID32/>
- ³⁴O. Robach, G. Renaud, and A. Barbier, *Surf. Sci.* **401**, 227 (1998).
- ³⁵R. Lazzari, *J. Appl. Crystallogr.* **35**, 406 (2002).
- ³⁶C. Revenant, F. Leroy, R. Lazzari, G. Renaud, and C. R. Henry, *Phys. Rev. B* **69**, 035411 (2004).
- ³⁷R. Lazzari and I. Simonsen, *Thin Solid Films* **419**, 124 (2002), and references therein.
- ³⁸R. Lazzari, G. Renaud, C. Revenant, J. Jupille, and Y. Borensztein, *Phys. Rev. B* **79**, 125428 (2009).
- ³⁹P. A. Mulheran and D. A. Robbie, *Europhys. Lett.* **49**, 617 (2000).
- ⁴⁰A. Trampert, F. Ernst, C. P. Flynn, H. F. Fischmeister, and M. Rühle, *Acta Metall. Mater.* **40**, S227 (1992).
- ⁴¹S. K. Sinha, E. B. Sirota, S. Garoff, and H. B. Stanley, *Phys. Rev. B* **38**, 2297 (1988).
- ⁴²M. Rauscher, T. Salditt, and H. Spohn, *Phys. Rev. B* **52**, 16855 (1995).
- ⁴³M. Rauscher, R. Paniago, H. Metzger, Z. Kovats, J. Domke, J. Peisl, H.-D. Pfannes, J. Schulze, and I. Eisele, *J. Appl. Phys.* **86**, 6763 (1999).
- ⁴⁴F. Gonella, E. Cattaruzza, G. Battaglin, F. D'Acapito, C. Sada, P. Mazzoldi, C. Maurizio, G. Mattei, A. Martorana, A. Longo, and F. Zontone, *J. Non-Cryst. Solids* **280**, 241 (2001).
- ⁴⁵A. Naudon, D. Babonneau, D. Thiaudière, and S. Lequien, *Physica B* **283**, 69 (2000).
- ⁴⁶R. Reitinger, B. Sepiol, G. Vogl, B. Pfau, L.-M. Stadler, S. Stankov, F. Zontone, N. Spiridis, and J. Korecki, *J. Appl. Phys.* **102**, 034310 (2007).
- ⁴⁷S. V. Roth, M. Burghammer, C. Riekkel, P. Müller-Buschbaum, A. Diethert, P. Panagiotou, and H. Walter, *Appl. Phys. Lett.* **82**, 1935 (2003).
- ⁴⁸S. V. Roth, H. Walter, M. Burghammer, C. Riekkel, B. Lengeler, C. Schroer, M. Kuhlmann, T. Walther, A. Sehrbrock, R. Dominick, and P. Müller-Buschbaum, *Appl. Phys. Lett.* **88**, 021910 (2006).
- ⁴⁹I. Kovačević, B. Pivac, P. Dubček, H. Zorc, N. Radić, S. Bernstorff, M. Campione, and A. Sassella, *Appl. Surf. Sci.* **253**, 3034 (2007).
- ⁵⁰K. Salamon, O. Milat, M. Buljan, U. V. Desnica, N. Radić, P. Dubček, and S. Bernstorff, *Thin Solid Films* **517**, 1899 (2009).
- ⁵¹O. Plantevin, R. Gago, L. Vázquez, A. Biermanns, and T. H. Metzger, *Appl. Phys. Lett.* **91**, 113105 (2007).
- ⁵²C. Revenant, F. Leroy, G. Renaud, R. Lazzari, A. Létoublon, and T. Madey, *Surf. Sci.* **601**, 3431 (2007).
- ⁵³A. Liebsch, *Phys. Rev. B* **48**, 11317 (1993).
- ⁵⁴D. Bedeaux and J. Vliieger, *Optical Properties of Surfaces* (Imperial, London, 2001).
- ⁵⁵I. Simonsen, R. Lazzari, J. Jupille, and S. Roux, *Phys. Rev. B* **61**, 7722 (2000).
- ⁵⁶G. Haas, A. Menck, H. Brune, J. V. Barth, J. A. Venables, and K. Kern, *Phys. Rev. B* **61**, 11105 (2000).
- ⁵⁷S. Rohart, G. Baudot, V. Repain, Y. Girard, and S. Rousset, *J. Cryst. Growth* **275**, e203 (2005).
- ⁵⁸J. L. Viovy, D. Beysens, and C. M. Knobler, *Phys. Rev. A* **37**, 4965 (1988).
- ⁵⁹R. Lazzari, G. Renaud, J. Jupille, and F. Leroy, *Phys. Rev. B* **76**, 125412 (2007).
- ⁶⁰P. Jensen, H. Larralde, M. Meunier, and A. Pimpinelli, *Surf. Sci.* **412-413**, 458 (1998).
- ⁶¹M. Bartelt and J. Evans, *Surf. Sci.* **298**, 421 (1993).
- ⁶²B. J. Briscoe and K. P. Galvin, *Phys. Rev. A* **43**, 1906 (1991).
- ⁶³P. Meakin, *Rep. Prog. Phys.* **55**, 157 (1992).
- ⁶⁴S. V. Khare and T. L. Einstein, *Phys. Rev. B* **54**, 11752 (1996).
- ⁶⁵J. Carrey, J.-L. Maurice, F. Petroff, and A. Vaurès, *Phys. Rev. Lett.* **86**, 4600 (2001).
- ⁶⁶J. Carrey, J.-L. Maurice, F. Petroff, and A. Vaurès, *Surf. Sci.* **504**, 75 (2002).
- ⁶⁷G. Barcaro, A. Fortunelli, F. Nita, and R. Ferrando, *Phys. Rev. Lett.* **95**, 246103 (2005).
- ⁶⁸G. Wulff, *Z. Kristallogr.* **34**, 449 (1901).
- ⁶⁹R. Kaishew, Ph.D. Thesis, Arbeitstagung Festkörper Physik, 1952.
- ⁷⁰L. Vitos, A. V. Ruban, H. L. Skriver, and J. Kollar, *Surf. Sci.* **411**, 186 (1998).
- ⁷¹F. Didier and J. Jupille, *Surf. Sci.* **314**, 378 (1994).
- ⁷²J. H. Larsen, J. T. Ranney, D. E. Starr, J. E. Musgrove, and C. T. Campbell, *Phys. Rev. B* **63**, 195410 (2001).
- ⁷³U. Schönberger, O. K. Andersen, and M. Methfessel, *Acta Metall. Mater.* **40**, S1 (1992).
- ⁷⁴C. Li, R. Wu, A. J. Freeman, and C. L. Fu, *Phys. Rev. B* **48**, 8317 (1993).
- ⁷⁵T. Hong, J. R. Smith, and D. J. Srolovitz, *Acta Metall. Mater.* **43**, 2721 (1995).
- ⁷⁶M. W. Finnis, *J. Phys.: Condens. Matter* **8**, 5811 (1996).
- ⁷⁷J. Purton, S. C. Parker, and D. W. Bullet, *J. Phys.: Condens. Matter* **9**, 5709 (1997).
- ⁷⁸G. Ehrlich and F. G. Hudda, *J. Chem. Phys.* **44**, 1039 (1966).
- ⁷⁹R. L. Schwoebel and E. J. Shipsey, *J. Appl. Phys.* **37**, 3682 (1966).
- ⁸⁰P. Jensen and N. Combe, *Comput. Mater. Sci.* **24**, 78 (2002).
- ⁸¹N. Combe, P. Jensen, and A. Pimpinelli, *Phys. Rev. Lett.* **85**, 110 (2000).